The Astrophysical Journal, 929:86 (9pp), 2022 April 10 https://doi.org/10.3847/1538-4357/ac5043
© 2022. The Author(s). Published by the American Astronomical Society.
OPEN ACCESS

The Decoupled Kinematics of High-z QSO Host Galaxies and Their Lyα Halos

Alyssa B. Drake[1,2], Marcel Neeleman[1], Bram P. Venemans[1], Mladen Novak[1], Fabian Walter[1], Eduardo Bañados[1], Roberto Decarli[3], Emanuele Paolo Farina[4], Chiara Mazzucchelli[5], and Maxime Trebitsch[1]
[1] Max Planck Institute für Astronomie, Königstuhl, Heidelberg, Germany; drake@mpia.de
[2] Centre for Astrophysics Research, Department of Physics, Astronomy and Mathematics, University of Hertfordshire, Hatfield AL10 9AB, UK
[3] INAF—Osservatorio Astronomico di Bologna, Via Piero Gobetti, 93/3, I-40129 Bologna BO, Italy
[4] Max Planck Institute for Astrophysics, Karl-Schwarzschild-Straße, Garching, Germany
[5] European Southern Observatory, Alonso de Cordova 3107, Vitacura, Region Metropolitana, Chile
Received 2021 February 23; revised 2022 January 17; accepted 2022 January 26; published 2022 April 15

Abstract

We present a comparison of the interstellar medium traced by [C II] (Atacama Large Millimeter/submillimeter Array), and ionized halo gas traced by Lyα (Multi Unit Spectroscopic Explorer), in and around QSO host galaxies at $z\sim6$. To date, 18 QSOs at this redshift have been studied with both MUSE and high-resolution ALMA imaging; of these, 8 objects display a Lyα halo. Using data cubes matched in velocity resolution, we compare and contrast the spatial and kinematic information of the Lyα halos and the host galaxies' [C II] (and dust-continuum) emission. We find that the Lyα halos extend typically 3−30 times beyond the interstellar medium of the host galaxies. The majority of the Lyα halos do not show ordered motion in their velocity fields, whereas most of the [C II] velocity fields do. In those cases where a velocity gradient can be measured in Lyα, the kinematics do not align with those derived from the [C II] emission. This implies that the Lyα emission is not tracing the outskirts of a large rotating disk, which is a simple extension of the central galaxy seen in [C II] emission. It rather suggests that the kinematics of the halo gas are decoupled from those of the central galaxy. Given the scattering nature of Lyα, these results need to be confirmed with James Webb Space Telescope Integral Field Unit observations that can constrain the halo kinematics further using the nonresonant Hα line.

Unified Astronomy Thesaurus concepts: Quasars (1319); Supermassive black holes (1663); Lyman-alpha galaxies (978)

Supporting material: figure sets

1. Introduction

High-redshift quasars (QSOs) present a unique opportunity to study some of the most extreme objects in the Universe, back to <1 Gyr after the Big Bang. In these objects vast amounts of material are funneled onto galaxies' central supermassive black holes. This leads to accretion disks that shine with sufficiently high luminosities to allow their detection well into the epoch of reionization (e.g., Mortlock et al. 2011; Bañados et al. 2018; Yang et al. 2020). At $z\sim6$, several hundred QSOs have now been detected (e.g., Bañados et al. 2016; Jiang et al. 2016; Mazzucchelli et al. 2017) and it was recently discovered that some of these QSOs are surrounded by giant Lyα halos. Drake et al. (2019) for instance presented deep Multi Unit Spectroscopic Explorer (MUSE) observations of 5 QSOs at $z\sim6$, and revealed that 4 of these objects displayed Lyα halos comparable in extent and luminosity to their lower redshift counterparts at $2\leqslant z\leqslant3$ (e.g., Borisova et al. 2016; Arrigoni Battaia et al. 2019). This confirmed earlier evidence of Lyα halos at $z\sim6$ based on long-slit spectroscopy and/or narrow-band imaging for both the radio-loud QSO J2228+0110 at $z=5.903$ (Zeimann et al. 2011; Roche et al. 2014) and J2329−0301 at $z=6.43$ (Goto et al. 2009, 2012; Willott et al. 2011 and Momose et al. 2019) and was later followed-up by Farina et al. (2019) who presented additional Lyα halos as part of the MUSE snapshot survey, Reionization Epoch Quasar Investigation with MUSE (REQUIEM).

Contemporaneously, observations from the Atacama Large Millimeter/submillimeter Array (ALMA) have revealed the far-infrared (FIR) dust-continuum and [C II] emission from the interstellar medium (ISM) in $\geqslant$27 $z\sim6$ quasar host galaxies (Decarli et al. 2017). These observations confirmed earlier studies in that these objects are rich in gas and dust. Higher spatial-resolution observations from ALMA reaching a resolution of ∼1 pkpc have been analyzed in a series of papers: these observations revealed centrally concentrated dust emission around the supermassive black holes (traced by FIR continuum emission; Venemans et al. 2020) and a diverse set of kinematics traced by [C II] emission (Neeleman et al. 2021) broadly split into three categories of equal number; disturbed, dispersion-dominated, or smoothly rotating. The third paper, Novak et al. (2020), determined that both [C II] and dust-continuum morphologies can be described with a two-component model consisting of a central steep component and an extended component of shallower gradient. While for the compact components the FIR continuum emission is more compact than the [C II], the extended components of both tracers extend over similar scales.

Despite the growing wealth of information now available for these objects, we have few constraints on the flow of gas into and around QSO host galaxies, and also the mechanisms governing the supply of pristine gas available to their rapidly accreting supermassive black holes. Indeed it is a long-standing question for simulations how the cold gas that is funneled along filaments connects to and feeds galaxies. Some numerical simulations have suggested that large Lyα halos will trace high

Original content from this work may be used under the terms of the Creative Commons Attribution 4.0 licence. Any further distribution of this work must maintain attribution to the author(s) and the title of the work, journal citation and DOI.

Table 1
Quasars at $z \sim 6$ Observed with Both ALMA and MUSE

Object	R.A. (ICRS)	Decl. (ICRS)	z	$L_{[\mathrm{C\,II}]}$ $10^8 L_\odot$	L_{FIR} $10^{11} L_\odot$	$L_{\mathrm{Ly}\alpha}$ erg s^{-1}	$d_{[\mathrm{C\,II}]}$ pkpc	d_{FIR} pkpc	$d_{\mathrm{Ly}\alpha}$ pkpc
J0129-0035	022.4938	−0.5944	5.7788	1.92 ± 0.07	4.76 ± 0.11	<1e+42	1.74 ± 0.17	1.10 ± 0.06	⋯
J1044-0125	161.1377	−1.4172	5.7846	1.64 ± 0.21	5.48 ± 0.22	<1e+42	1.88 ± 0.58	0.94 ± 0.12	⋯
P007+04	007.0274	04.9571	6.0015	1.58 ± 0.09	4.52 ± 0.11	<2e+42	1.30 ± 0.23	0.65 ± 0.11	⋯
P009–10	009.7355	−10.4317	6.0040	9.07 ± 0.66	7.13 ± 0.69	9e+42	4.04 ± 0.57	3.03 ± 0.46	20.40 ± 2.15
J2054-0005	313.5271	−0.0874	6.0389	3.08 ± 0.14	6.20 ± 0.19	<1e+42	1.37 ± 0.11	0.79 ± 0.06	⋯
J2100-1715	315.2279	−17.2561	6.0807	1.31 ± 0.14	1.12 ± 0.16	<1e+42	1.67 ± 0.45	1.30 ± 0.00	⋯
J2318-3029	349.6379	−30.4927	6.1456	2.22 ± 0.12	6.29 ± 0.14	<1e+42	1.24 ± 0.11	0.75 ± 0.06	⋯
P359–06	359.1352	−6.3831	6.1719	2.62 ± 0.13	1.60 ± 0.15	3.3e+43	2.10 ± 0.22	1.88 ± 0.28	20.09 ± 2.12
P065–26	065.4085	−26.9544	6.1871	1.71 ± 0.17	2.80 ± 0.23	6.6e+43	4.33 ± 0.95	1.10 ± 0.39	20.07 ± 2.11
P308–21	308.0416	−21.2340	6.2355	3.37 ± 0.19	2.45 ± 0.16	8.8e+43	3.14 ± 0.56	3.20 ± 0.56	30.64 ± 3.23
J0100+2802	015.0543	28.0405	6.3269	3.76 ± 0.17	2.92 ± 0.18	<5e+42	2.41 ± 0.55	1.84 ± 0.44	⋯
J025-33	025.6822	−33.4627	6.3373	5.65 ± 0.22	5.31 ± 0.24	<3e+42	2.06 ± 0.17	1.28 ± 0.11	⋯
P183+05	183.1124	05.0926	6.4386	7.15 ± 0.32	10.53 ± 0.36	<6e+42	3.29 ± 0.27	2.14 ± 0.11	⋯
J2318-3113	349.5765	−31.2296	6.4429	1.59 ± 0.14	0.79 ± 0.17	<2e+42	3.32 ± 0.71	2.57 ± 1.65	⋯
P036+03	036.5078	03.0498	6.5405	3.38 ± 0.09	5.77 ± 0.12	3.8e+43	1.96 ± 0.11	0.89 ± 0.05	19.44 ± 2.05
P231–20	231.6577	−20.8336	6.5869	3.53 ± 0.30	9.99 ± 0.34	1.1e+44	1.02 ± 0.11	0.55 ± 0.05	29.69 ± 3.13
P323+12	323.1382	12.2986	6.5872	1.45 ± 0.19	0.53 ± 0.27	2.01e+44	2.04 ± 0.54	0.59 ± 0.00	45.52 ± 4.79
J0305-3150	046.3205	−31.8488	6.6139	5.90 ± 0.36	12.30 ± 0.44	8e+42	2.70 ± 0.22	1.60 ± 0.11	12.60 ± 1.33

Note. We list here: object names (column 1), coordinates (columns 2 and 3), systemic redshift from [C II] ($z_{[\mathrm{C\,II}]}$; column 4), and three luminosities $L_{[\mathrm{C\,II}]}$ (column 5) and L_{FIR} (column 6) from Venemans et al. (2020), and $L_{\mathrm{Ly}\alpha}$ (column 7) from Farina et al. (2019). In the final three columns we list the diameter d of the [C II], FIR, and Lyα halo components reported in Venemans et al. (2020) and Farina et al. (2019). $d_{[\mathrm{C\,II}]}$ (column 8) and d_{FIR} (column 9) are the geometric averages of a 2D Gaussian fit, and $d_{\mathrm{Ly}\alpha}$ (column 10) is the diameter at which the surface-brightness-dimming-corrected light profile drops below 3×10^{-18} erg s^{-1} cm^{-2} arcsec^{-2}.

angular-momentum gas as it is accreted (e.g., Stewart et al. 2011 and Stewart et al. 2013)—observational evidence for this scenario is found in Prescott et al. (2015), where the authors report large-scale rotation of a collapsing gas structure. To date, no further rotation of gas in emission on this scale has been presented in the literature. It is prudent then, to compare and contrast available data sets, to gain insights on the relationship between the kinematics of the ISM inside QSO host galaxies and extended Lyα halos tracing ionized gas around them (likely to be connected to the circumgalactic medium, CGM; e.g., Drake et al. 2019; Farina et al. 2019).

In this work we examine $z \sim 6$ QSOs observed with high-resolution ALMA configurations to compare and contrast the bright, central emission from the host galaxies (the core-like component reported in Novak et al. (2020) and examined in Venemans et al. (2020)) to observations of the same QSOs with MUSE as part of the REQUIEM survey (Farina et al. 2019) which have reported the presence/absence of Lyα halos (tracing gaseous reservoirs) down to 5σ surface-brightness limits of $(0.1\text{–}1.1) \times 10^{-17}$ erg s^{-1} cm^{-2} arcsec^{-2} over a 1 arcsec^2 aperture. This paper proceeds as follows. In Section 2 we describe the observations and data sets compiled for this work. In Section 3 we present [C II] and Lyα channel maps and moment maps of our targets. In Section 4 we discuss our findings and comment on our targets individually. Finally, in Section 5 we summarize our findings.

Throughout this work we assume a ΛCDM cosmology with $\Omega_m = 0.3$, $\Omega_\Lambda = 0.7$ and $H_0 = 70$ km s^{-1} Mpc^{-1}. In this cosmology, $1'' = 5.71$ pkpc at $z \approx 6$. All velocities, wavelengths, and frequencies refer to vacuum values.

2. Observations and Sample Selection

2.1. Sample Selection

We draw our sample from a total of 18 sources that represent the overlap between the high-resolution ALMA [C II] imaging survey published in Venemans et al. (2020) and the MUSE REQUIEM survey (Farina et al. 2019). We list the full sample in Table 1 before defining a subset where a Lyα halo detection has been made in Drake et al. (2019) and Farina et al. (2019). The sample with robust detections in both data sets amounts to eight objects.

2.2. MUSE Data

MUSE data cubes are taken from the REQUIEM survey (Farina et al. 2019) in order to homogenize the reduction process across all objects. Farina et al. (2019) define the Lyα halo as a 3D structure of connected voxels of significance $>2\,\sigma$ after smoothing the point-spread function (PSF)-subtracted datacube in the spatial and spectral directions with kernels of $\sigma_{\mathrm{spat}} = 0.''2$ and $\sigma_{\mathrm{spec}} = 2.5$ Å. The study also provides moment maps for the Lyα halos, with a velocity zero-point that refers to the flux-weighted centroid of the voxels included in the mask. For the purpose of this work, we require moment maps centered on systemic velocity, and so we utilize additional data products released with REQUIEM to construct our own maps, as described in Section 3.1.

2.3. ALMA Data

ALMA data cubes of the continuum-subtracted [C II] emission line are taken from Decarli et al. (2017) and Venemans et al. (2019, 2020). The data have been reimaged with natural weighting to maximize sensitivity to any extended emission, and sampled with a velocity width of 30 MHz per channel to match the velocity width of a single layer of the (slightly oversampled) MUSE datacube (∼40 km s^{-1}). All data cubes were observed in the local standard of rest velocity frame.

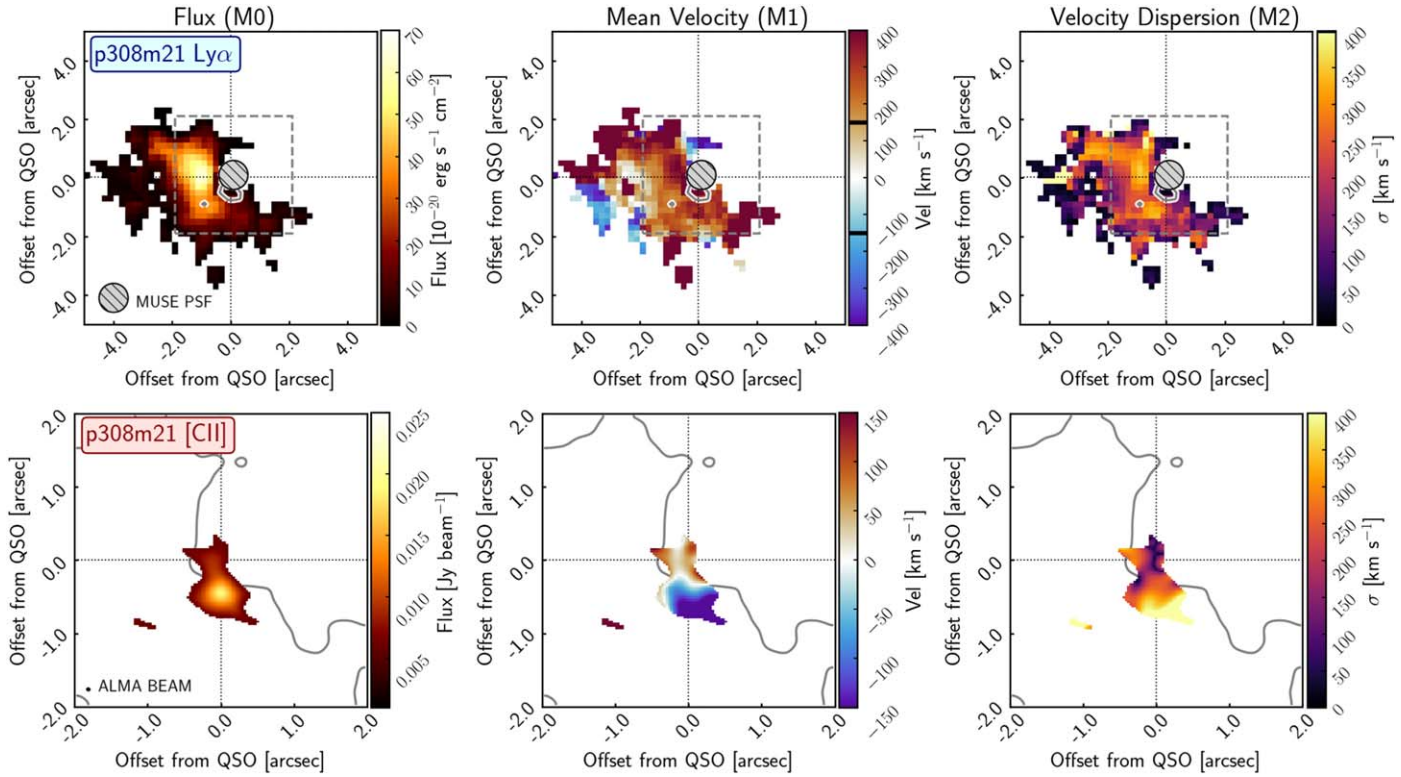

Figure 1. Moment maps for the Lyα halo (upper panels) and [C II] emission (lower panels) for P308–21. The upper panels are 10″ a side. The area corresponding to complex residuals following PSF-subtraction is shown by the hatched circle. In addition, gray contours show the region from which the [C II] emission is mapped. The lower panels zoom in to a box of 4″ a side (gray dashed boxes in the top row), and display the [C II] moment maps together with a gray contour that traces the edge of the Lyα halo (shown above). The left column shows the flux images (moment 0), the central column shows the velocity offset relative to systemic z (moment 1; note that the color bar for the lower panels is a zoom-in to the range shown by two black bars on the color bar in the upper panels), and the right column shows the velocity dispersion (σ, moment 2) of the gas. Moment maps for the full sample can be found in the figure set (eight components) available in the online journal.

(The complete figure set (8 images) is available.)

3. Results

3.1. Moment Maps

As we require the velocity fields (moment 1) to describe ionized gas motion relative to the systemic velocity of the host galaxy (defined as the [C II] redshift), we utilize two data products released with the REQUIEM survey: the PSF-subtracted data cubes, and the 3D mask cubes to reconstruct the 3D Lyα halo as defined in Farina et al. (2019). With these cubes we then recompute moment maps relative to systemic velocity, using the method applied in Drake et al. (2020).

In Figure 1 we show an example of the Lyα and [C II] moment maps for P308–21. Maps for the full sample can be found in the figure set available in the online journal. The three columns of panels present the zeroth moment (total flux), the first moment (velocity field), and the second moment (a measure of the velocity dispersion), respectively. The upper row of panels focuses on the Lyα halo in cutouts of 10″ a side, while the lower panels present [C II] emission originating in the quasar host galaxy in panels which zoom-in to 4″ a side.

An immediate takeaway from this comparison is the relative sizes of the extended halo gas traced by Lyα, and the more compact [C II] emission which traces the host galaxy. Typically, the extent of the [C II] emission is encompassed within the region of $\sim$1″ diameter, which corresponds to the region of the Lyα emission that is subject to complex residuals due to the PSF-subtraction (here, this region is masked on the Lyα images). We will return to size comparison in Section 4.1 where measurements for the full sample will be considered.

The central columns of Figure 1 depicting the velocity fields of the emission demonstrate a general feature of the data: there is no obvious coherence between the velocity field of the host galaxy and that of the extended ionized gas for any of the eight objects. We will discuss this further in Section 4.2. We also note that a comparison of the general velocity shifts is presented in Section 5.1.1. and Figure 5 of Farina et al. (2019).

3.2. Channel Maps

In addition to the moment analysis of gas kinematics for each object, we include in the Appendix a series of channel maps comparing Lyα and [C II] emission for each QSO. In every case, the Lyα extends over a much greater velocity range than the more compact [C II] emission, and the maps emphasize again the extent of the gaseous ionized halo gas compared to the cold gas in the host galaxy.

4. Discussion

4.1. Size Comparison

In Figure 2 we compare the sizes of the [C II] and FIR continuum emission to that of the Lyα halo. The adopted size measurements are listed in Table 1. For the Lyα size we take the surface-brightness-dimming-corrected size from Farina et al. (2019; their method 4) for consistency of method across

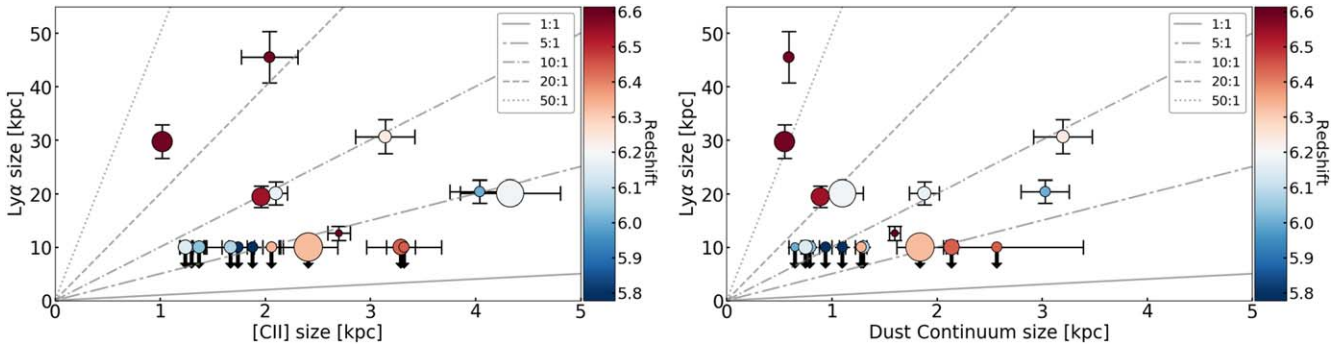

Figure 2. Size comparison between the host galaxy in [C II] (left panel), FIR dust continuum (right panel), and the Lyα halo. The [C II] and FIR sizes are adapted from Venemans et al. (2020), and the Lyα sizes are taken from Farina et al. (2019) and represent the diameter of each halo. The size of each symbol represents its black hole mass, with the values taken from Schindler et al. (2020). The diagonal gray lines represent lines of constant size ratio between the Lyα halo and the host galaxy. Downward arrows represent objects undetected in Lyα for which we assume a maximum size of 10 pkpc.

all objects and redshifts. For the [C II] and FIR sizes we take values from Venemans et al. (2020), where sizes from the Common Astronomy Software Applications (CASA) task IMFIT are provided using a 2D fit. In this work we take the geometric average of these two measurements as the effective [C II] or FIR extent.

The two panels show on the x-axes the [C II] size (left side) and FIR dust continuum (right size) against the Lyα extend on the y-axes. As was evident from Figure 1, the Lyα halos are significantly more extended than the [C II] (and also dust-continuum) emission. This is because the [C II] emission primarily traces photodominated regions within the host galaxy, meanwhile, the extended Lyα emission traces the extended ionized gas surrounding the central host galaxy.

Lyα halo sizes fall anywhere between $\sim$2 and $\sim$30 times larger than the [C II] sizes. P009–10 at $z = 6.00$ shows the smallest Lyα halo, four times larger than its extended [C II], which stretches $\sim$4 pkpc. At the other end of the scale, P231–20, at $z = 6.59$ has a Lyα halo extending $\approx$30 times further than its compact [C II] emission which is measured at 1 pkpc. In the right panel we confirm that the FIR (tracing the dust-continuum) is smaller than the [C II] size (e.g., see Novak et al. 2020 for a detailed analysis of [C II] and FIR dust-continuum sizes). The Lyα halos range between $\sim$3 and $>$50 times larger than the dust continuum. Much as for the [C II] comparison, P009–10 exhibits the lowest size ratio of $d_{\mathrm{Ly}\alpha}/d_{\mathrm{FIR}} = 5$, and again, P231–20 exhibits the largest size ratio of $d_{\mathrm{Ly}\alpha}/d_{\mathrm{FIR}} = 67$. Interestingly, in the FIR, P323+12 moves up the ranking and exhibits the second largest size ratio of $d_{\mathrm{Ly}\alpha}/d_{\mathrm{FIR}} = 61$. Additional information is encoded in the figure, using QSO redshift to color the data points and scaling the size of each point by the QSO's supermassive black hole mass (taken from Schindler et al. 2020). No correlation is seen between M_{BH} and any of the size measures (Lyα, [C II], or FIR), nor with the ratio of Lyα halo size to host-galaxy tracer size. A Kendall's rank correlation test (accounting for upper limits) shows that there is no evidence for a correlation between the [C II]/FIR and Lyα halo sizes.

In Figure 3 we consider the ratio of sizes between the Lyα halo and the two tracers of the galaxy's ISM as a function of redshift. Neither the Lyα/[C II] size, nor the Lyα/FIR size shows any correlation with redshift ($\tau = 0.067$ with $p = 0.42$, and $\tau = 0.04$ with $p = 0.40$, respectively)—this implies no evolution of the size ratio across our redshift range.

4.2. Kinematic Comparison

We now compare the overall kinematics of the ISM in the host galaxy, traced by [C II], with the larger-scale kinematics as traced by the Lyα line. The underlying question is whether the bulk motion between the two tracers is the same, i.e., if they trace the same gravitationally bound structure. We acknowledge that the gas kinematics traced by Lyα are difficult to interpret due to the complex radiative transfer of Lyα photons that may prevent a clear kinematic signature.

By comparing the [C II] velocity fields to those of the Lyα line we find, to first order, no evidence for coherent rotation between these two tracers. In many cases this is due to the fact that the Lyα velocity field does not show a clear velocity gradient. The [C II], on the other hand, does indeed show such a velocity gradient in the majority of sources (Neeleman et al. 2021). There are three cases, discussed in detail below, where we see a clear gradient in the velocity field of the Lyα halos; these are P359–06, P036+03, and P231–20. In the notes below, we use the commonly adopted definition of the position angle (P.A.)—the angle measured from north, counterclockwise, to the receding part of the emission.

4.2.1. Notes on the Kinematics of Individual Objects

4.2.2. P009–10

Given the asymmetric extended [C II] emission, Venemans et al. (2020) speculate that P009–10 may be in the process of merging with another source. Examining the moment maps in Figure 1, P009–10's elongation in [C II] aligns with the orientation of the Lyα halo. In terms of kinematics, a velocity gradient is seen along the [C II] emission, meanwhile an obvious gradient in the Lyα halo is absent.

4.2.3. P359–06

The [C II] emission from P359–06 is surrounded by a Lyα halo. The kinematics of P359–06 in [C II] show a velocity gradient approximately from east to west (P.A. of $315\overset{\circ}{.}7 \pm 2\overset{\circ}{.}6$; Neeleman et al. 2021), meanwhile the kinematic structure of the surrounding Lyα halo does not appear to be aligned, with a mild gradient from north to south and additional blueshifted emission in the southern outskirts.

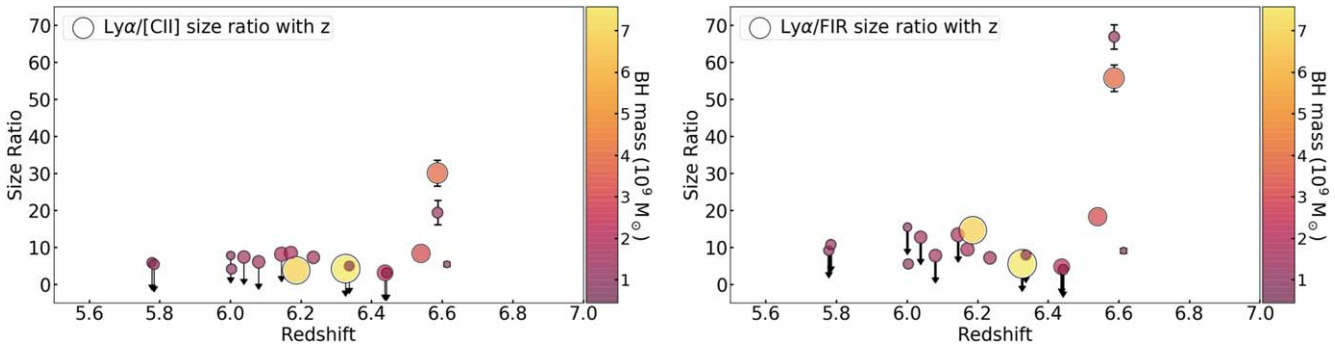

Figure 3. Size ratio between the Lyα halo and [C II] (left panel)/FIR dust continuum (right panel) as a function of redshift. Symbol sizes and colors encode the black hole mass, and the downward arrows represent objects undetected in Lyα for which we assume a maximum size of 10 pkpc.

4.2.4. P065–26

Venemans et al. (2020) note that the [C II] morphology of P065–26 is extended and disturbed. The Lyα halo surrounds the [C II], with a marginal extension toward the north. The kinematics show no obvious velocity gradient across the structure, but simply patches of mildly blue- and redshifted emission. In contrast, the entirety of the Lyα halo appears to be blueshifted by a few hundred km s^{-1}.

4.2.5. P308–21

P308–21 is extended in both [C II] and Lyα emission. The [C II] emission has been extensively studied in Decarli et al. (2019) with high-resolution imaging. The authors argue that the extended tails of [C II] emission are due to the tidal stripping of a satellite galaxy. In the moment maps, we see that the Lyα halo is much larger still than the extended [C II]. The peak of the Lyα emission is in the northeastern direction from the peak in [C II], which is centered on the QSO position. The [C II] emission from the QSO host galaxy shows a velocity gradient in the south–north direction. The Lyα halo meanwhile is redshifted across almost the entirety of the structure, except for the very outskirts of the halo in the east.

4.2.6. P036+03

P036+03 shows a relatively compact [C II] morphology, and a Lyα halo extending toward the north. The [C II] emission shows a gradient from north to south (P.A. $189\overset{\circ}{.}9^{+1.8}_{-2.0}$; Neeleman et al. 2021), meanwhile the Lyα halo shows a gradient that is approximately perpendicular to this (from east to west, with an approximate P.A. of $\approx$270°). P036+03 presents the most striking contrast between the halo and ISM velocity fields of the objects studied here.

4.2.7. P231–20

P231–20 has a gas-rich companion detected in [C II], presented in Decarli et al. (2017), 9 kpc south of the QSO, and a second, fainter, companion, presented in Neeleman et al. (2019). The [C II] emission that is associated with the quasar is compact, and Neeleman et al. (2021) report a P.A. of 83° ± 4°. The Lyα halo is present prominently toward the north of the QSO. There is a pronounced velocity gradient in the east–west direction across the Lyα halo, with a P.A. of approximately $\approx$315°.

4.2.8. P323+12

P323+12 shows very compact and faint [C II] emission. In contrast, its Lyα halo is bright, and is one of the more extended of the sample. The [C II] kinematics do not show a velocity gradient, and the majority of the Lyα halo is blueshifted.

4.2.9. J0305–3150

J0305–3150 was first presented in Venemans et al. (2016), and supplemented with very high-resolution data in Venemans et al. (2020), resolving scales of $\sim$400 pc. The Lyα halo was the first $z \sim 6$ halo reported with MUSE, presented in Farina et al. (2017). Neither the [C II] emission nor the Lyα halo are particularly luminous. In terms of kinematics, the [C II] displays a clear gradient from the southwest to the northeast. The Lyα halo within which it is embedded is redshifted in its entirety, extending mainly to the south.

5. Summary

We have presented a comparison of Lyα and [C II] emission of a sample of eight QSOs at $z \sim 6$, using MUSE and ALMA data cubes matched in velocity resolution. The [C II] emission traces the extent and kinematics of the interstellar medium of the QSO host galaxy, whereas the Lyα emission traces the extent and kinematics of the ionized gaseous halos that surround the quasar hosts.

We find that the Lyα halo sizes are typically 3–30 times larger than the extent of the [C II] that is associated with the host galaxy (and 3–60 times larger than the host galaxy's dust-continuum emission). A comparison of the kinematics has proven more difficult, as the majority of the Lyα halos do not show ordered motion in their velocity fields. In those three cases where a kinematic P.A. can be determined in the respective Lyα halos, their velocity fields are not aligned with that of the [C II] emission. In other words, we find not a single case where the rotational signature associated with the host galaxy extends to the Lyα halo. This suggests that the Lyα emission is not simply tracing the outskirts of a large rotating disk structure that is a simple extension of the central structure seen in [C II] (and dust) emission. It rather suggests that the kinematics of the halo gas are decoupled from those of the interstellar medium in the host galaxies' disks.

Connecting the kinematics of [C II] and Lyα remains a challenge, in particular in the presence of companions and/or asymmetries in the gas distribution. An additional caveat is that, given its highly scattering nature, the Lyα emission line is not an ideal tracer for gas kinematics. While we do not think

this should affect our ability to detect rotational signatures at large galacto-centric radii, a confirmation of our results will have to await observations of the sources with the NIRSpec Integral Field Unit on board the James Webb Space Telescope. Ideally, a large sample of isolated sources is required to investigate the general case of cosmological accretion using the Hα emission line, allowing a direct and unambiguous comparison of the halo kinematics to those of the host galaxy in [C II].

We would like to thank the anonymous referee for the constructive comments which have greatly helped to improve the paper. A.B.D., F.W., M.N., and M.N. acknowledge support from the ERC Advanced Grant 740246 (Cosmic Gas). A.B.D. also acknowledges support from the UK Science and Technology Facilities Council (STFC) under grant ST/V000624/1.

Appendix
Channel Maps of Lyα and [C II] Emission

We include here in Figure 4 a series of channel maps depicting emission from [C II] in the QSO host galaxies, and Lyα in the extended halos extracted at the same velocity. The [C II] emission in each panel is that arising in a single channel of 30 MHz ($\sim$40 km s^{-1}), in comparison the Lyα emission from the slightly oversampled MUSE datacube is the sum across a 2 Å wide window ($\sim$66 km s^{-1}). All panels are cutouts of 10″ a-side, with the exception of the highest redshift object, J0305–3150 where the very high-resolution observations from ALMA dictate that we zoom in to panels of 6″ a-side, and remove the masking of PSF residuals in the Lyα image in order to see the host galaxy in [C II] in these maps. Channel maps for the full sample can be found in the figure set available in the online journal.

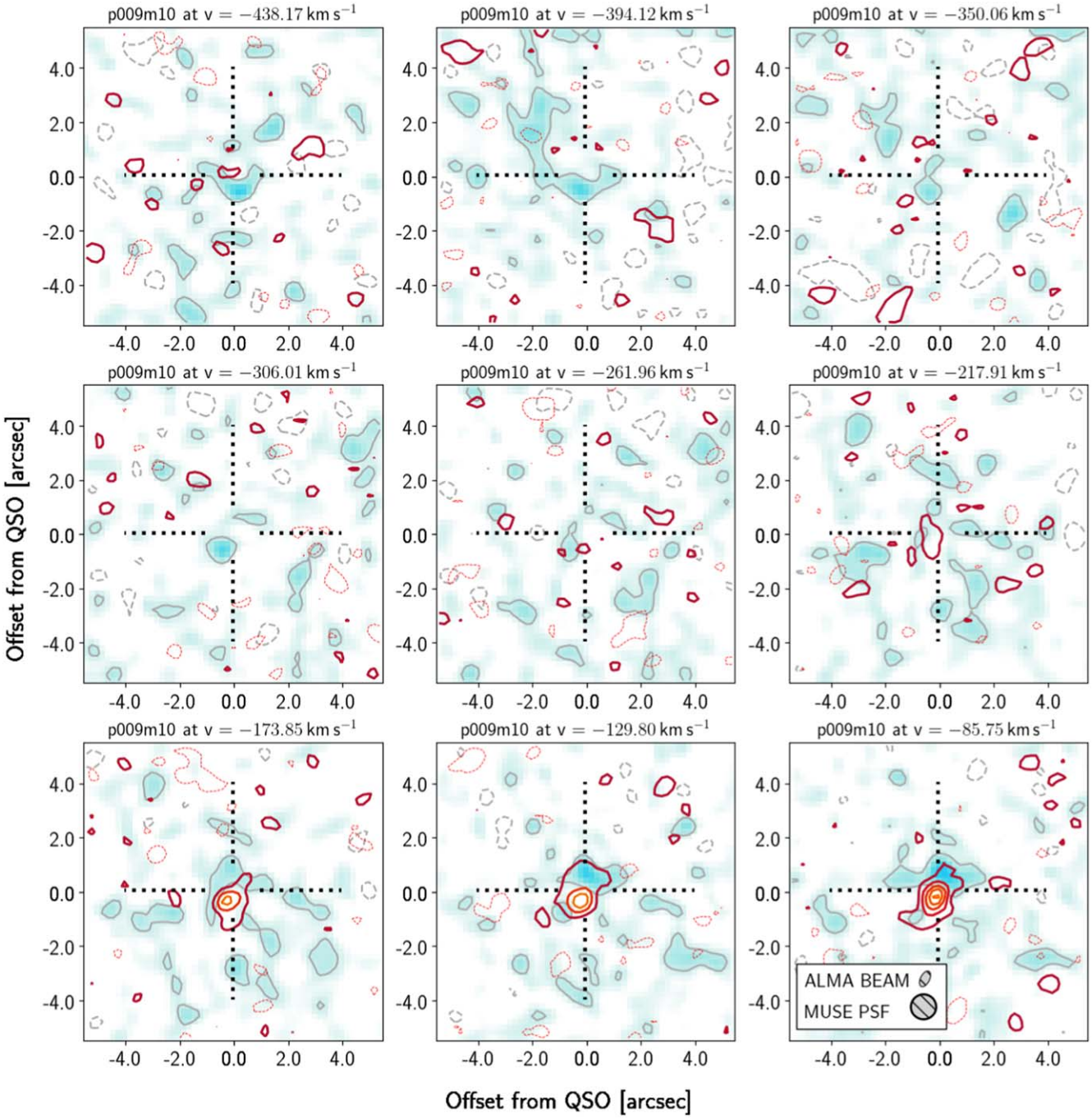

Figure 4. Channel maps displaying images of extended Lyα emission overlaid with linearly spaced contours depicting [C II] emission at the same velocity. The lowest positive (solid) and negative (dashed) contour levels represent $\pm 2\sigma$ ($\pm 4\sigma$ for J0305–3150) in the [C II] channel after smoothing with a Gaussian kernel of FWHM = 2.23 pixels. The [C II] emission in each panel is that arising in a single channel of 30 MHz ($\sim$40 km s^{-1}), in comparison, the Lyα emission from the slightly oversampled MUSE datacube is the sum across a 2 Å wide window ($\sim$66 km s^{-1}). The Lyα image is smoothed with a Gaussian kernel of FWHM= 3.30 pixels and contoured at $\pm 1.5\sigma$ (solid, dashed lines). This demonstrates that an extended low-surface-brightness component is contiguous over multiple velocity channels. We present two pages of channel maps for each object in turn, beginning with the lowest redshift quasar, P009–10. Channel maps for the full sample can be found in the figure set (eight components) available in the online journal.

(The complete figure set (8 images) is available.)

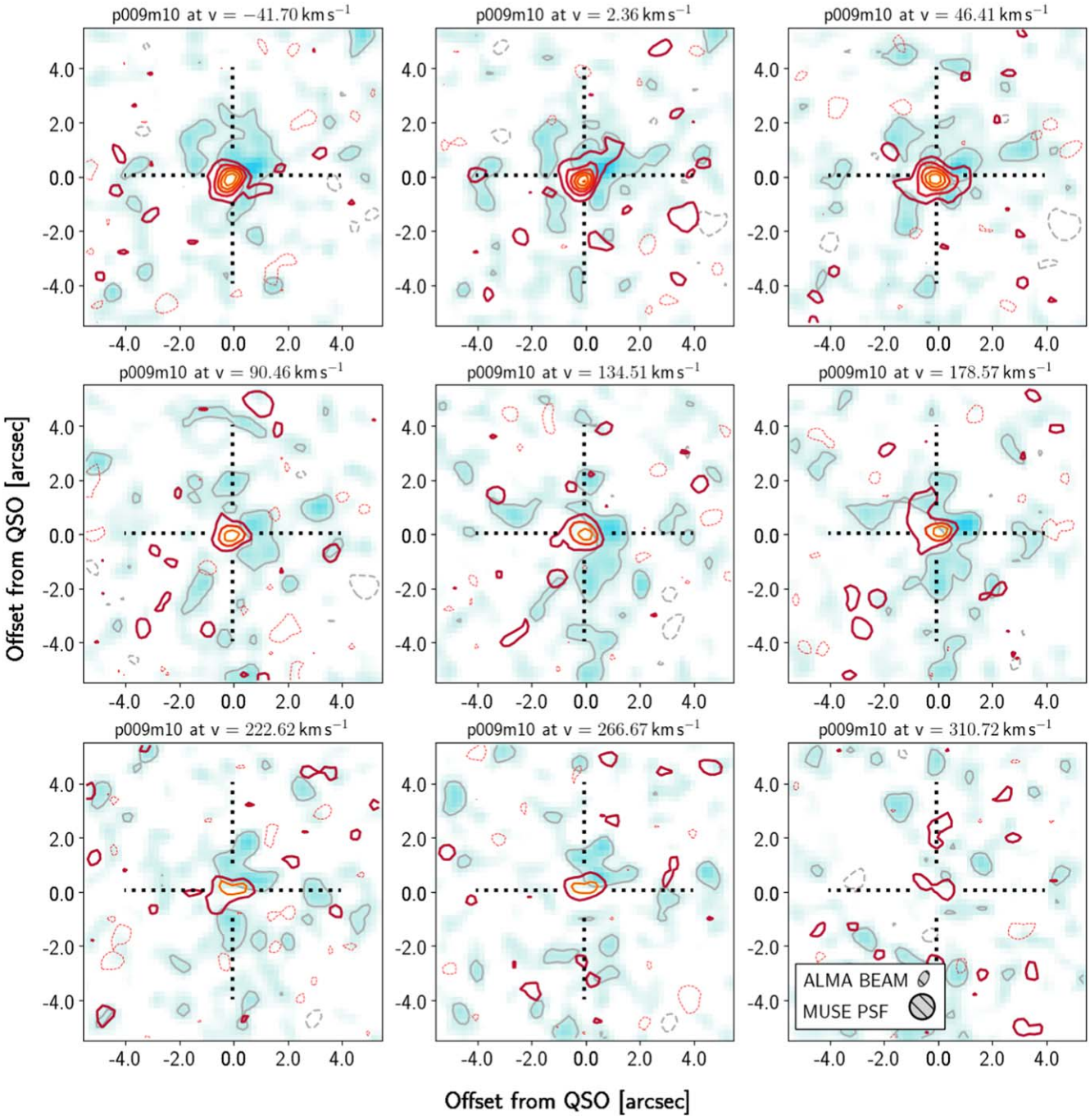

Figure 4. (Continued.)

ORCID iDs

Alyssa B. Drake https://orcid.org/0000-0002-0174-3362
Marcel Neeleman https://orcid.org/0000-0002-9838-8191
Bram P. Venemans https://orcid.org/0000-0001-9024-8322
Mladen Novak https://orcid.org/0000-0001-8695-825X
Fabian Walter https://orcid.org/0000-0003-4793-7880
Eduardo Bañados https://orcid.org/0000-0002-2931-7824
Roberto Decarli https://orcid.org/0000-0002-2662-8803
Emanuele Paolo Farina https://orcid.org/0000-0002-6822-2254
Chiara Mazzucchelli https://orcid.org/0000-0002-5941-5214
Maxime Trebitsch https://orcid.org/0000-0002-6849-5375

References

Arrigoni Battaia, F., Hennawi, J. F., Prochaska, J. X., et al. 2019, MNRAS, 482, 3162
Bañados, E., Venemans, B. P., Decarli, R., et al. 2016, ApJS, 227, 11
Bañados, E., Venemans, B. P., Mazzucchelli, C., et al. 2018, Natur, 553, 473
Borisova, E., Cantalupo, S., Lilly, S. J., et al. 2016, ApJ, 831, 39
Decarli, R., Dotti, M., Bañados, E., et al. 2019, ApJ, 880, 157
Decarli, R., Walter, F., Venemans, B. P., et al. 2017, Natur, 545, 457
Drake, A. B., Farina, E. P., Neeleman, M., et al. 2019, ApJ, 881, 131
Drake, A. B., Walter, F., Novak, M., et al. 2020, ApJ, 902, 37
Farina, E. P., Arrigoni-Battaia, F., Costa, T., et al. 2019, ApJ, 887, 196
Farina, E. P., Venemans, B. P., Decarli, R., et al. 2017, ApJ, 848, 78
Goto, T., Utsumi, Y., Furusawa, H., Miyazaki, S., & Komiyama, Y. 2009, MNRAS, 400, 843

Goto, T., Utsumi, Y., Walsh, J. R., et al. 2012, MNRAS, 421, 77
Jiang, L., McGreer, I. D., Fan, X., et al. 2016, ApJ, 833, 222
Mazzucchelli, C., Bañados, E., Venemans, B. P., et al. 2017, ApJ, 849, 91
Momose, R., Goto, T., Utsumi, Y., et al. 2019, MNRAS, 488, 120
Mortlock, D. J., Warren, S. J., Venemans, B. P., et al. 2011, Natur, 474, 616
Neeleman, M., Bañados, E., Walter, F., et al. 2019, ApJ, 882, 10
Neeleman, M., Novak, M., Venemans, B. P., et al. 2021, ApJ, 911, 141
Novak, M., Venemans, B. P., Walter, F., et al. 2020, ApJ, 904, 131
Prescott, M. K. M., Martin, C. L., & Dey, A. 2015, ApJ, 799, 62
Roche, N., Humphrey, A., & Binette, L. 2014, MNRAS, 443, 3795
Schindler, J.-T., Farina, E. P., Bañados, E., et al. 2020, ApJ, 905, 51
Stewart, K. R., Brooks, A. M., Bullock, J. S., et al. 2013, ApJ, 769, 74
Stewart, K. R., Kaufmann, T., Bullock, J. S., et al. 2011, ApJ, 738, 39
Venemans, B. P., Neeleman, M., Walter, F., et al. 2019, ApJL, 874, L30
Venemans, B. P., Walter, F., Neeleman, M., et al. 2020, ApJ, 904, 130
Venemans, B. P., Walter, F., Zschaechner, L., et al. 2016, ApJ, 816, 37
Willott, C. J., Chet, S., Bergeron, J., & Hutchings, J. B. 2011, AJ, 142, 186
Yang, J., Wang, F., Fan, X., et al. 2020, ApJL, 897, L14
Zeimann, G., Richard, L. W., Becker, R. H., et al. 2011, ApJ, 736, 57